

## ENGINEERING

## Instant, multiscale dry transfer printing by atomic diffusion control at heterogeneous interfaces

Seungkyoung Heo<sup>1,2†</sup>, Jeongdae Ha<sup>1,2†</sup>, Sook Jin Son<sup>3</sup>, In Sun Choi<sup>3</sup>, Hyeokjun Lee<sup>1,2</sup>,  
 Saehyuck Oh<sup>1,2</sup>, Janghwan Jekal<sup>1,2</sup>, Min Hyung Kang<sup>4</sup>, Gil Ju Lee<sup>4</sup>, Han Hee Jung<sup>1,2</sup>,  
 Junwoo Yea<sup>1,2</sup>, Taeyoon Lee<sup>5</sup>, Youngjeon Lee<sup>2,6</sup>, Ji-Woong Choi<sup>2,7</sup>, Sheng Xu<sup>8</sup>, Joon Ho Choi<sup>2,3</sup>,  
 Jae-Woong Jeong<sup>2,9</sup>, Young Min Song<sup>4</sup>, Jong-Cheol Rah<sup>2,3\*</sup>, Hohyun Keum<sup>10\*</sup>, Kyung-In Jang<sup>1,2,3\*</sup>

Transfer printing is a technique that integrates heterogeneous materials by readily retrieving functional elements from a grown substrate and subsequently printing them onto a specific target site. These strategies are broadly exploited to construct heterogeneously integrated electronic devices. A typical wet transfer printing method exhibits limitations related to unwanted displacement and shape distortion of the device due to uncontrollable fluid movement and slow chemical diffusion. In this study, a dry transfer printing technique that allows reliable and instant release of devices by exploiting the thermal expansion mismatch between adjacent materials is demonstrated, and computational studies are conducted to investigate the fundamental mechanisms of the dry transfer printing process. Extensive exemplary demonstrations of multiscale, sequential wet-dry, circuit-level, and biological topography-based transfer printing demonstrate the potential of this technique for many other emerging applications in modern electronics that have not been achieved through conventional wet transfer printing over the past few decades.

## INTRODUCTION

Research on thin-film electronics (1–8) in which functional elements are integrated on unusual substrates has drawn much attention and has established the foundation for flexible electronic systems. These approaches can surpass the mechanical constraints of conventional wafer-oriented fabrication processes while yielding high device performance by using inorganic materials with physicochemical stability and electrical properties as functional elements. The unique attributes of these material designs, such as flexibility, stretchability, and bendability, facilitate a variety of electronic device applications. Specific examples include flexible displays (9, 10), flexible optoelectronics (11–14), wireless communication systems (15, 16), bio-integrated electronics (17–25), and many other advanced applications that are not directly accessible with current wafer-based electronics.

In the typical semiconductor fabrication of thin-film electronics, pliable substrates composed of organic materials or polymers hinder the direct growth of inorganic materials, since their unstable thermal properties lead to degradation or damage of the substrate from the extreme process conditions. An effective alternative is the preparation of inorganic materials on rigid growth substrates in a releasable

state and subsequent delivery onto the desired target substrates. The transfer printing technique (26–29) can be used for this process, which empowers the heterogeneous integration of different classes of materials in spatially organized layouts.

One of the most common transfer printing techniques is wet transfer printing, which removes sacrificial intermediate layers through chemical reactions. This process readily picks up and prints the functional components in engineered configurations with high throughput. In addition, advanced methods of programmable transfer printing have recently been developed using laser and heat-deformable stamp (30, 31). These methods make transfer printing easier and more sophisticated. However, in the wet transfer printing method, the aqueous etchant adopted for sacrificial layer dissolution can distort the shapes of device patterns through flotation due to uncontrollable fluidic motion, which makes it difficult to precisely control the retrieval of the devices and match their initial arrangements. In addition, since the prolonged process time associated with the diffusion of chemical etchants limits the dimensions of the releasable patterns to the micrometer scale, this method is not suitable for transfer printing of delicate designs or large areas.

Several dry transfer printing methods have recently been developed to overcome the disadvantages of wet transfer printing. A recent study demonstrated a dry transfer printing method that separates the device from the substrate by exploiting the weak adhesion between polydimethylsiloxane (PDMS) and polyimide (PI) (32). This method has the advantage of being facile and rapid. However, the method is limited in that the susceptibility of the PDMS layer to heat precludes the substrate from being subjected to a high-temperature process. Another method has been proposed based on laser irradiation (33). Laser irradiation weakens the adhesion between the substrate and the device by inducing a phase transition for a-Si. This method can eliminate pattern distortion and facilitate rapid processing. However, laser equipment is essential for delamination of the device. Furthermore, the substrate is limited to transparent substrate.

<sup>1</sup>Department of Robotics Engineering, Daegu Gyeongbuk Institute of Science and Technology, Daegu 42988, South Korea. <sup>2</sup>Brain Engineering Convergence Research Center, Daegu Gyeongbuk Institute of Science and Technology, Daegu 42988, South Korea. <sup>3</sup>Korea Brain Research Institute, Daegu 41062, South Korea. <sup>4</sup>School of Electrical Engineering and Computer Science, Gwangju Institute of Science and Technology, Gwangju 61005, South Korea. <sup>5</sup>Department of Electrical and Electronic Engineering, Yonsei University, Seoul 03722, South Korea. <sup>6</sup>National Primate Research Center, Korea Research Institute of Bioscience and Biotechnology, Cheongju, Chungcheongbuk-do 28116, South Korea. <sup>7</sup>Department of Information and Communication Engineering, Daegu Gyeongbuk Institute of Science and Technology, Daegu 42988, South Korea. <sup>8</sup>Department of Nanoengineering, University of California San Diego, La Jolla, CA 92093-0448, USA. <sup>9</sup>School of Electrical Engineering, Korea Advanced Institute of Science and Technology, Daejeon 34141, South Korea. <sup>10</sup>Korea Institute of Industrial Technology, Cheonan, 31056 South Korea.

\*Corresponding author. Email: kijang@dgist.ac.kr (K.-I.J.); hkeum@kitech.re.kr (H.K.); jcrh@kbri.re.kr (J.-C.R.)

†These authors contributed equally to this work.

Here, dry transfer printing, which exploits the intrinsic material properties and overcomes the limitations of the aforementioned transfer printing, is proposed. This type of transfer printing uses the apparent difference between the coefficients of thermal expansion (CTE) of dissimilar adjacent materials. When the substrate and the device layer expand due to the heating process, the thermal expansion mismatch between them maximizes the stress at the interface in conjunction with interfacial edge cracking, which has a decisive effect on the device release. Computational analysis and experimental results explore the physics underlying the exfoliation of device from the substrate due to thermal stress. Compared to wet transfer printing, which dissolves the material, dry transfer printing enables multi-scale, high-throughput, and time-efficient transfer printing using the inherent CTE values of the material. The fabrication of wireless transmitters, optogenetic devices, embedded systems for healthcare and environmental monitoring, and bio-integrated sensors shows the great potential of the proposed technique to fabricate thin-film electronics in widespread applications.

## RESULTS

### Dry transfer printing

Figure 1 (A and B) schematically illustrates the main principle of dry transfer printing along with a brief procedure and the multilayer structures. The process begins with the placement of a thin metal layer that has a CTE greater than that of the substrate, such as silicon (Si) and glass. Microstructures corresponding to the device layer in the schematics are prepared on the metal layer with a conventional surface micromachining process. Applying heat to the device induces thermal stress at the interface between the underlying substrate and device layer. The thermal stress leads to crack propagation at the interface. After a thermal cycle consisting of heating and cooling, the microcracks facilitate physical exfoliation of the device layer with adhesive tape.

The design of multilayer construction for dry transfer printing is strongly dependent on the intrinsic material properties of the metal layer. Two types of approaches categorized according to the level of atomic diffusion during the heating process are used. The first approach is illustrated in Fig. 1A, where a thin film device can be prepared on a gold (Au)/Si layer and readily delaminated from the substrate by controlling the thermal stress while avoiding undesired atomic diffusion and associated Au silicide (34) at the interface (fig. S1). The second case is illustrated in Fig. 1B, where copper (Cu), which is vulnerable to thermal atomic diffusion, is used, and an antiatomic diffusion layer is required, for example, through surface modification of the Si substrate with silane-based self-assembled monolayers (SAMs) (35). As shown in the x-ray photoelectron spectroscopic (XPS) analysis in fig. S2, the surface-treated Si substrate and the Cu layer can be elementally separated without leaving any residue on each surface.

The proposed dry transfer printing bypasses the principal limitations of the traditional wet transfer printing process (fig. S3) of prolonged release (etch) time and shape distortion driven by the wet etching of the sacrificial layer (36). Figure 1C demonstrates that the release time of dry transfer printing is more than six orders of magnitude faster than that of wet transfer printing. Including the total consumption time with thermal cycles, a few seconds are sufficient for dry transfer printing. A shape distortion comparison between the proposed dry transfer printing and traditional wet

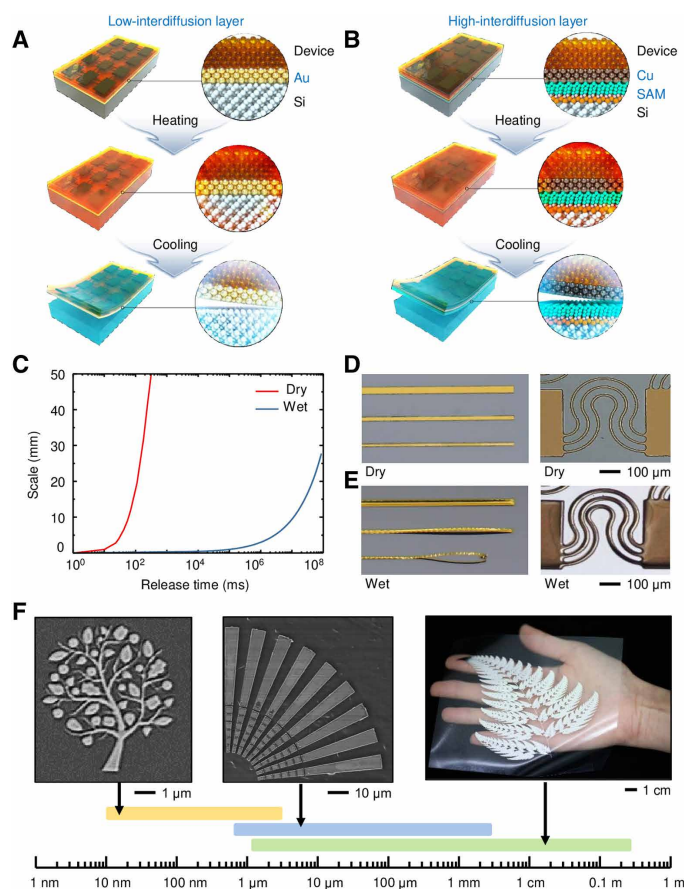


**Fig. 1. Dry transfer printing by interfacial thermal stress control and antiatomic diffusible interface design.** (A) Schematic illustration of the process for dry transfer printing depending on the atomic diffusion level of the material with a high CTE. The process is classified into a low-interdiffusion layer (Au) and (B) a high-interdiffusion layer (Cu), necessitating an antiatomic diffusion layer. (C) Computational and theoretically calculated results for the scale-release time correlation of wet and dry transfer printing denoted by the blue line and red line, respectively. Dry transfer printing takes only a few hundred milliseconds to release submeter-scale patterns. (D) Optical images of line and serpentine patterns in the dry transfer printing process and (E) pattern floating and distortion in the wet transfer printing process. Photo credit: Seungkyoung Heo, Daegu Gyeongbuk Institute of Science and Technology. (F) Optical images of patterns with diverse shapes (tree pattern, radial pattern, and fern leaf fractal pattern) from the nanometer scale to the submeter scale by dry transfer printing. Photo credit: Seungkyoung Heo, Daegu Gyeongbuk Institute of Science and Technology.

transfer printing is experimentally demonstrated. As shown in Fig. 1D, dry transfer printing maintains the original shape of the microstructures after the release process. On the other hand, wet transfer printing yields undesired floating and wrinkling of the micropatterns during the wet etching process of the sacrificial layer, resulting in disordered settlement on the substrate (Fig. 1E and fig. S4). Dry transfer printing also exhibits outstanding scalability regardless of the pattern size or shape with the help of its rapid release time and fluid-free release method. As shown in Fig. 1F and figs. S5 and S6, the ultrawide geometrical scalability enables instant transfer printing from the nanometer scale to a scale of a few sub-meters, which is unattainable by the conventional transfer printing

method. In addition, fig. S7 demonstrates that dry transfer printing can be integrated with widely used adhesive transfer printing tools.

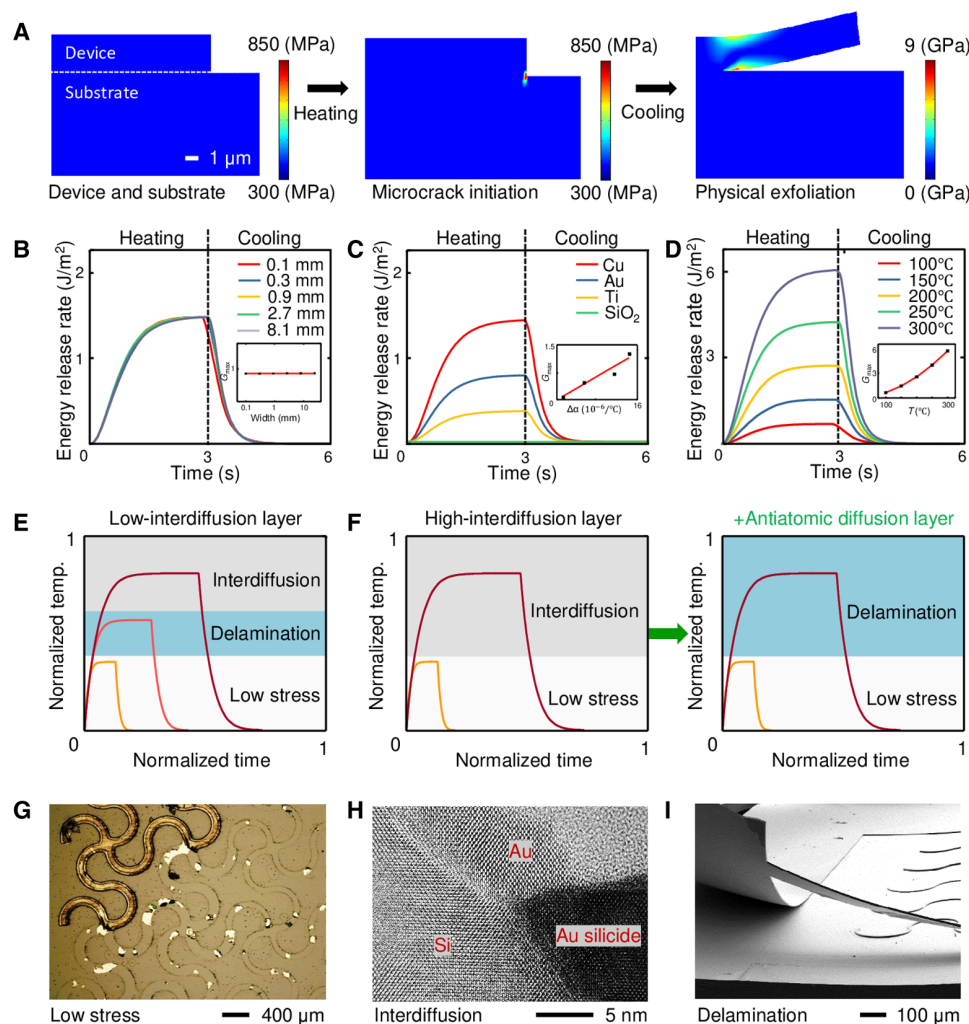
### Thermomechanics of dry transfer printing

Figure 2 (A to D) shows the finite element analysis (FEA) results for the investigation of thermal stress, energy release rate, and crack initiation during the dry transfer printing process. The cohesive zone model is selected as the fracture mechanics model and used for the FEA. The simulation parameters of the FEA are listed in table S1.

The substrate consists of Si (100 mm in diameter; 525  $\mu\text{m}$  in thickness). The device comprises three distinct layers of Au (200 nm), PI (1  $\mu\text{m}$ ), and a Cu device layer (200 nm) with a width of 2 cm. The delamination process for dry transfer printing is divided into two steps: (i) microcrack initiation at the edge of the interface and (ii) entire physical exfoliation by using an adhesive transfer printing tool, as shown in Fig. 2A. The thermal stress caused by the CTE mismatch

induces microcracks at the edge of the interface during the heating process. The thermal stress is sharply increased at the edge (37), and the region where the stress is concentrated is extremely narrow, as shown in fig. S8. After cooling, there is no residual thermal stress at the interface. The exfoliation stress becomes concentrated at the crack tip while the device is exfoliated by using adhesive tape. The microcracks are ordinarily smaller than 1  $\mu\text{m}$ , but the existence of the microcracks plays a critical role in the stress concentration during the physical exfoliation step. When microcracks exist at the edge of the interface, the stress is highly concentrated around the crack tip according to the Griffith theory (38), allowing exfoliation even under low exfoliation stress.

The energy release rate resulting from the microcrack initiation step is depicted in Fig. 2 (B to D). Regardless of the lateral width of the device, magnitudes of the maximum energy release rate are almost the same as shown in Fig. 2C. This trend demonstrates that



**Fig. 2. Thermomechanics of dry transfer printing.** (A) Consecutive schematic diagram of the stress distribution during the crack initiation and physical exfoliation steps. (B) Energy release rate for different widths of the device during the thermal cycle. (C) Energy release rate for different materials of the device layer during the thermal cycle. (D) Energy release rate for different heating temperatures during the thermal cycle. Schematic diagrams of thermal delamination approaches using (E) a low-interdiffusion layer and (F) a high-interdiffusion layer. (G) Delamination failure due to low stress and the corresponding optical image. Photo credit: Seungkyoung Heo, Daegu Gyeongbuk Institute of Science and Technology. (H) Delamination failure due to Au silicide formation and the corresponding transmission electron microscopy image. Photo credit: Seungkyoung Heo, Daegu Gyeongbuk Institute of Science and Technology. (I) Successful delamination with atomic diffusion control and the corresponding SEM image. Photo credit: Seungkyoung Heo, Daegu Gyeongbuk Institute of Science and Technology.



microcracks develop along the boundaries of the device layer regardless of the lateral width of the device.

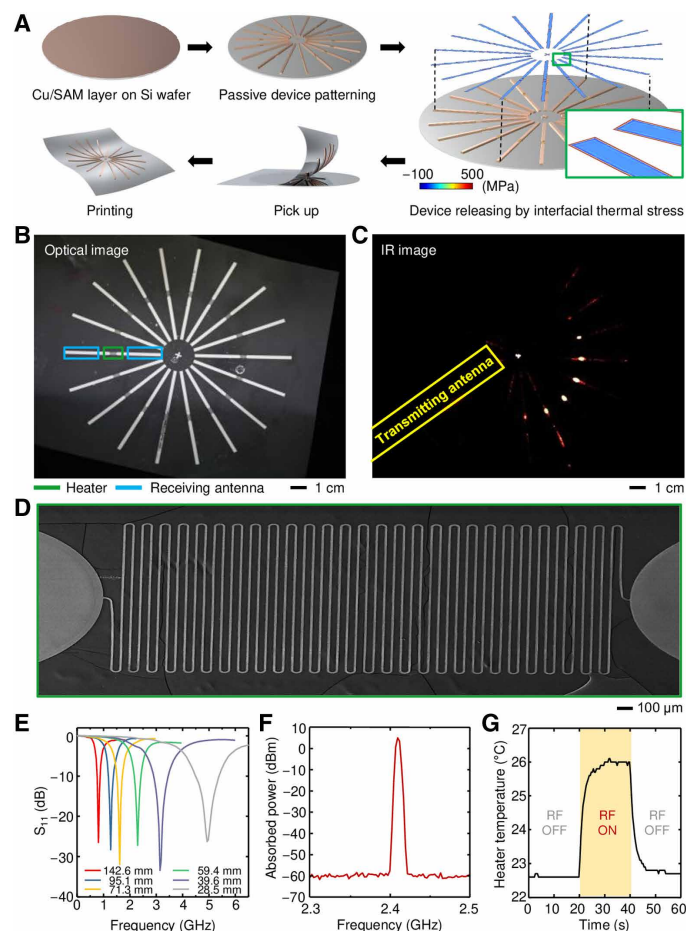
The energy release rate rapidly increases and becomes saturated at a certain level in the heating phase and decreases in a similar fashion in the cooling phase. The maximum energy release rate is proportional to the CTE mismatch between the substrate (Si) and device layer (Cu, Au, Ti, or SiO<sub>2</sub>), as described in Fig. 2C. In addition to the CTE, the heating temperature affects the energy release rate. Figure 2D and the corresponding inset depict positive linear relationship of the heating temperature and the magnitude of the energy release rate. This tendency indicates that crack initiation can easily occur at high temperatures. However, excessively high heating temperatures make physical exfoliation difficult owing to atomic interdiffusion between the Si substrate and device layer.

Figure 2E is a schematic diagram of the thermal delamination strategy in the case of a low-interdiffusion layer (e.g., Au). In this case, the heterogeneous interface exhibits not only microcracks but also atomic interdiffusion, as shown in Fig. 2H. Atomic interdiffusion inhibits physical delamination by forming unwanted Au silicide or Cu silicide at heterogeneous interfaces. Furthermore, the formation of metal silicide results in the loss of thermo-reversibility of the device layer, which may cause buckling. In contrast, at relatively low temperatures, since the thermal stress at the edge of the interface is insufficient for the generation of microcracks, the initial cracks are not fully induced, and delamination is not perfectly carried out, as shown in Fig. 2G. Therefore, in this approach, it is important to control the heating temperature within a specific regime where cracks initiate but interdiffusion does not appear. On the other hand, materials with a high atomic diffusion coefficient (e.g., Cu) are vulnerable to interdiffusion even in a low-temperature regime. Figure 2F shows a schematic diagram of the other thermal delamination approach, which bypasses the interdiffusion problem by adopting an antiatomic diffusion layer as a chemical diffusion barrier. In this case, the anti-interdiffusion layer is placed between the substrate and the device layer. Active inhibition of interdiffusion by using an anti-interdiffusion layer allows successful delamination, as shown in Fig. 2I.

### Multiscale dry transfer printing

Multiscale patterning of the micro/nanostructures in large areas is widely used for high-throughput industrial devices such as modern electronic devices. The dry transfer printing in this study is suitable for such micro/nanofeatures with meso-scale patterns since it uses the intrinsic material properties instead of aqueous etching. In this experiment, radial arrays of submeter-scale dipole antennas with a micrometer-scale electroresistive heater are fabricated by the dry transfer printing technique.

As depicted in Fig. 3A, a Cu/SAM bilayer is adopted as a release layer to apply thermal stress and prevent atomic diffusion to the substrate. The patterned multiscale antenna arrays are simultaneously physically retrieved from the substrate using the thermal stress induced between the antiatomic diffusion layer-coated Si substrate and the Cu layer underneath the wireless heater during the dry transfer printing process. The optical and scanning electron microscope (SEM) images of the fabricated devices in Fig. 3 (B and D) show that dry transfer printing covers the deterministic transfer printing of multiscale patterns containing a few micrometers of wireless heaters (highlighted by the green box, Fig. 3D) and a few centimeters of dipole antenna patterns (highlighted by the blue box). The performance of the wireless heater prepared by dry transfer printing is



**Fig. 3. Wireless heater by multiscale dry transfer printing.** (A) Schematic illustration of the fabrication process for a wireless heater using multiscale dry transfer printing. FEA corresponding to wireless heater patterns formed on a Si wafer, where the colored box represents the von Mises stress concentrated at the edge of the device during the heating process. (B) Optical images of a wireless heater with multiscale patterns composed of a microheater (highlighted in the green colored box) and dipole antenna (highlighted in the blue colored box), which are dry-transferred onto transparent adhesive tapes. Photo credit: Seungkyoung Heo, Daegu Gyeongbuk Institute of Science and Technology. (C) IR images of the wireless heater during exposure to external electromagnetic energy. Selective heating occurs in heaters parallel to the direction of releasing factor (RF) energy radiation among radially arranged heater arrays. Photo credit: Seungkyoung Heo, Daegu Gyeongbuk Institute of Science and Technology. (D) SEM images of fine microheater patterns with a linewidth of 20  $\mu\text{m}$ . Photo credit: Seungkyoung Heo, Daegu Gyeongbuk Institute of Science and Technology. (E)  $S_{11}$  of a wireless heater with different antenna lengths. (F) Absorbed electrical power measured from an individual antenna at a resonant frequency of 2.4 GHz. (G) Transient behavior in the temperature of the heater element under wireless electromagnetic irradiation. The irradiation of RF energy controls the temporal heating and cooling features of the heater.

verified through wireless power transmission and infrared (IR) imaging (fig. S9). When exposed to radiation from external electromagnetic waves, the receiving antenna absorbs radio frequency (RF) energy at its resonant frequency, which generates oscillating current and associated thermal energy by Joule heating at the heater element (Fig. 3C).

The different lengths of dipole antenna arrays are designed and fabricated in the same manner (fig. S10). In Fig. 3E, each receiving

antenna exhibits resonance in a specific frequency corresponding to its designed length, which proves that dry transfer printing provides extensive scalability for multiscale resonant frequency antennas. As shown in Fig. 3F, the absorbed electrical power through the receiving antenna exhibits a sharp peak at its resonant frequency. Figure 3G shows that the temperature of the heater immediately increases under irradiation from external electromagnetic energy and returns to the initial temperature as soon as RF energy is turned off, which demonstrates the wireless instant temperature control capability of the heater.

### Sequential wet-dry transfer printing

The sequential wet-dry transfer printing demonstrated here refers to a combinatory process technique that involves typical wet transfer printing of active microscale components onto metal interconnects to establish a functional device that is subsequently released from the rigid substrate through dry transfer printing to give the device a flexible form factor. These sequential process steps are beneficial when the course of fabrication involves exceedingly high temperatures for the construction of high-performance functional elements such as light-emitting diodes (LEDs) or photodetectors (PDs) integrated with multiscale electrical interconnects.

As a demonstrative application of sequential wet-dry transfer printing, an epidermal electronic device for cardiovascular monitoring is fabricated, and its process sequence is presented in Fig. 4A. Individual fabrication (39, 40) of the active optoelectronic components ( $\mu$ -ILEDs and  $\mu$ -Si PD) provides spatially ordered arrays of micro/nanostructures suspended on each epitaxial growth substrate (GaAs and Si on insulator wafer) with photoresist (PR) anchors (figs. S11 and S12). The reversible control of the van der Waals adhesion against the elastomeric stamp enables selective retrieval of the optoelectronic components from their donor substrates and printing of the component onto the target substrate prepared with a partially cured PI adhesive layer over Au/Si. As shown in the process flow (fig. S13), metal traces interconnect the printed components after hole formation, and the entire device is fully packaged with a dielectric passivation layer. The device fabricated on the Au/Si substrate is designed to exhibit thermal stress, which is selectively concentrated at the edges of the interface, as shown in the FEA, and eventually facilitates the physical exfoliation of the device from the substrate. Figure S14 shows optical images of the photoplethysmography (PPG) sensor prepared by sequential wet-dry transfer printing. To prepare cardiovascular monitoring, an epidermal electrocardiography (ECG) sensor consisting of fine serpentine lines and electric contact pads is additionally fabricated using dry transfer printing (fig. S15). The fabricated epidermal cardiovascular monitor enables real-time measurement of the ECG, PPG, and desired pulse wave velocity (PWV), which is a critical medical indicator of vascular stiffness and distensibility (Fig. 4B). Simultaneous measurements of the pulse waves from the central arteries to the peripheral arteries and the ECG enable the calculation of the time interval between them, which identifies the pulse arrival time (PAT). The epidermal device makes intimate contact with curvilinear surfaces because of its low mechanical modulus and stretchable design (Fig. 4C).

The ECG sensor and PPG sensor are mounted on the chest and fingertip, respectively, for the real-time measurement of the PAT (fig. S16). Figure 4 (D and E) shows the ECG and PPG signals and the corresponding PAT between these signals. The epidermal cardiovascular monitor also measures the hemodynamics of the blood

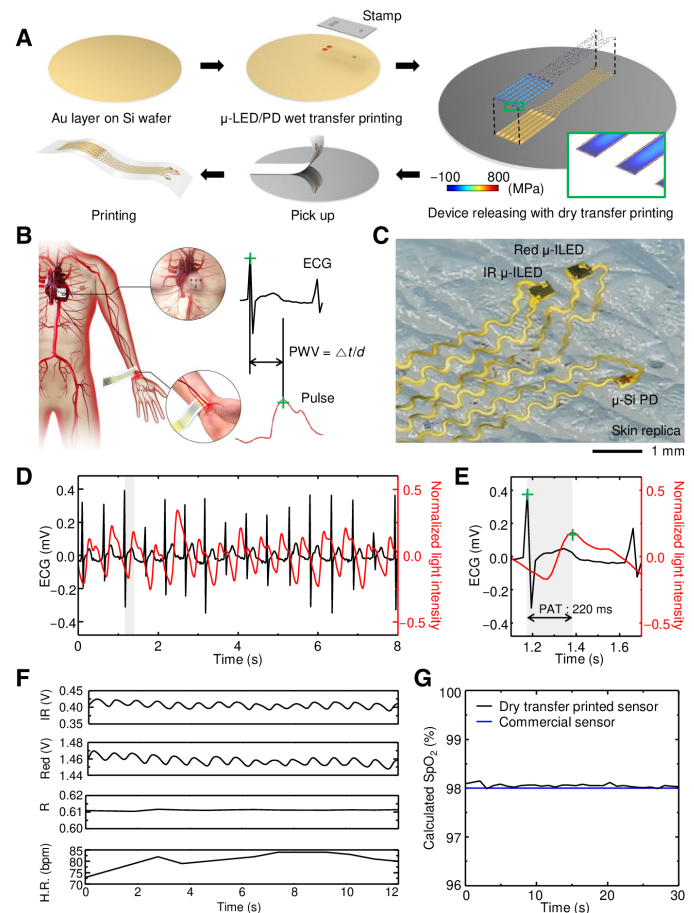


**Fig. 4. Epidermal cardiovascular monitor with sequential wet-dry transfer printing.** (A) Schematic illustration of the fabrication process for epidermal cardiovascular monitoring using sequential wet-dry transfer printing. (B) Illustration of PWV measurement by simultaneous PPG and ECG measurements from epidermal sensors. Photo credit: Seungkyoung Heo, Daegu Gyeongbuk Institute of Science and Technology. (C) Optical images of the epidermal PPG sensor with active components ( $\mu$ -ILEDs and  $\mu$ -Si PD) and serpentine interconnections compliantly laminated on the human skin replica. Photo credit: Seungkyoung Heo, Daegu Gyeongbuk Institute of Science and Technology. (D) Measurement results for pulse and ECG. (E) Calculation of PAT from the time interval between peaks of each waveform highlighted in the gray zone. (F) Light intensity signals of the PD element. Calculated  $R$  values from the pulsatile (AC) component and nonpulsatile (DC) component in each light intensity signal. Calculated heart rate from the waveform period of the collected light intensity signals. (G) Comparison of the  $\text{SpO}_2$  results from the dry transfer-printed PPG sensor and commercial pulse oximeter.

flow under the skin, as presented in Fig. 4F. In this case, the light modulation of red and IR LEDs in the PPG sensor allows selective light detection of each optical wavelength and calculation of the heart rate, measured red and IR signal modulation ratio ( $R$  value), and blood oxygen saturation ( $\text{SpO}_2$ ), considering the intrinsic absorption characteristics of the biological tissues and blood flow. In Fig. 4G, the  $\text{SpO}_2$  value derived from the  $R$  value matches that of a commercial pulse oximeter (41).

### Circuit-level dry transfer printing

Modern printed circuit board (PCB) technology facilitates the implementation of highly sophisticated embedded systems through

surface mounting technologies (SMTs), and PCBs with soft form factors have played a key role in emerging flexible electronic devices through their thin design and deformability. Convolved PCB design in soft architecture is inaccessible with the prevailing wet transfer printing process due to the problems associated with process time and feature misalignment, whereas dry transfer printing operates through convenient heat treatment. In this experiment, an embedded system for gas inhalation monitoring is demonstrated to show the suitability of dry transfer printing for the implementation of soft PCBs.

Figure 5A shows the manufacturing process of an embedded system containing integrated circuit (IC) chips. The circuit-level patterning of the metal interconnections on the Cu/SAM layer-coated Si wafer includes the electrical opening for chip mounting and encapsulation with dielectric materials (fig. S17). Figure 5B shows the complete exfoliation of the multilayer circuit patterns after the thermal stress release process. IC chips, including batteries, microcontroller units (MCUs), metal oxide semiconductor field-effect transistors (MOSFETs), multiplexers, accelerometers, and gas sensors, are

mounted on the corresponding electrical contacts, as shown in the optical image in Fig. 5C.

The fabricated device simultaneously monitors real-time information related to biological signals and environmental conditions to obtain gas inhalation values based on the circuit design depicted in fig. S18. For the measurement of gas inhalation, the fabricated embedded system is adhered on the chest of the subject, and the subject is exposed to smoke containing harmful carbon monoxide (CO) gas by placing a cigarette in the area (fig. S19). As depicted in Fig. 5D, the signals of the accelerometer present the tracking of the physical diaphragm movement followed by repetitive inhalations and exhalations, and the respiratory rate is calculated through the time interval between the peaks of the acceleration waveforms. Using the obtained values from each sensor and the inhalation volume of normal adult males (500 ml per respiration) determines the total amount of CO gas (240  $\mu\text{g}$ ) inhaled by the subject during the experimental period (30 min), which could be used in a wide range of embedded systems.

### Topography-based dry transfer printing

Dry transfer printing also enables fabrication of extremely thin large-scale flexible devices that are capable of precisely and conformably locating unconventional three-dimensional (3D) surfaces such as the brain. In this study, an optoelectronic skull patch that locally stimulates multiple specific regions of a mouse brain is demonstrated. To design the proposed device matched to the shape of the mouse skull, a 3D scanner precisely maps the spatial information of the individual motor cortex and reference bregma positions (Fig. 6A and fig. S20), based on which the optoelectronic device is designed two-dimensionally.

The optogenetic scalp patch, designed to locate the  $\mu\text{-LEDs}$  on the intact or cleared skull (42) of the corresponding stimulation sites (fig. S21), allows the individual manipulation of the optoelectronic elements (fig. S22). To conduct an *in vivo* test, channelrhodopsin-2 (ChR2), a blue light-gated cation channel, is stereotactically delivered through adeno-associated virus (AAV) into the primary and secondary motor cortex of wild-type mice. As shown in Fig. 6B and fig. S23, the thin and stretchable design of the device permits accommodation of the curved scalp topography and intimate optical contact between biotic and abiotic interfaces so that the interface can convey light without loss. To prove the practicality of the device as an optogenetic stimulator, a multichannel recording electrode is inserted into the motor cortex region. The electrode is inserted at a sharp angle ( $\sim 30^\circ$ ) so that the electrode can detect the neural activity stimulated by light through the cleared skull, as depicted in Fig. 6C and fig. S24. The target neurons show optogenetic stimulation and an intensity-dependent increase in the frequency of action potentials in response to various the light intensities of the optogenetic patch, as shown in Fig. 6 (D and E).

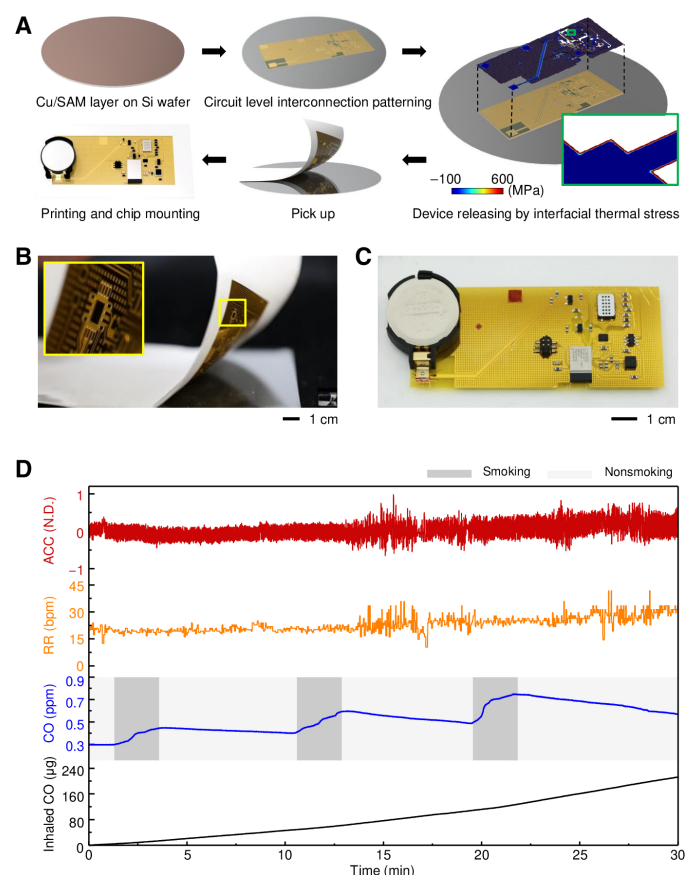


**Fig. 5. Wireless gas inhalation monitor with circuit-level dry transfer printing.**

(A) Schematic illustration of the fabrication process for a wireless gas inhalation monitor using circuit-level dry transfer printing. Photo credit: Seungkyoung Heo, Daegu Gyeongbuk Institute of Science and Technology. (B) Optical image of the circuit patterns transferred from the Si wafer with water-soluble tape. The magnified inset image at the top left shows the complete physical integrity of the pattern picked up during the exfoliation step. Photo credit: Seungkyoung Heo, Daegu Gyeongbuk Institute of Science and Technology. (C) Optical image of the device with the IC chip mounted. (D) Measured acceleration, respiratory rate, CO concentrations, and derived inhaled CO amounts for 30 min. N.D., NonDimensional.

### DISCUSSION

Recent advances in modern electronics have included the development of designs in which functional components are highly integrated into unusual platforms in response to tremendously advanced application needs. Wet transfer printing has conventionally been used for this heterogeneous integration but exhibits the drawbacks of uncontrollable feature distortion and prolonged process time because of the aqueous sacrificial layer removal process. Unlike wet transfer



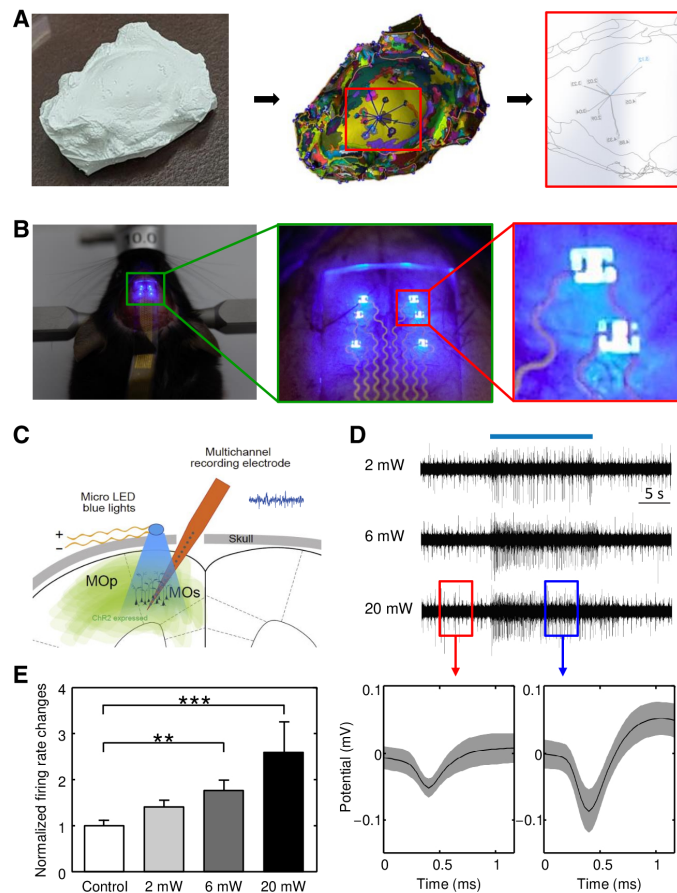


**Fig. 6. Scalp-mounted optogenetic stimulator with topography-based dry transfer printing.** (A) 3D scanning process of the mouse brain model for obtaining the spatial information of stimulus sites considering the biological anatomy. Photo credit: Seungkyoung Heo, Daegu Gyeongbuk Institute of Science and Technology. (B) Optical images of an optogenetic stimulator resting on the target positions of the mouse brain during the operation of the  $\mu$ -ILEDs and magnified optical images of a device with active components and stretchable interconnections. Photo credit: Seungkyoung Heo, Daegu Gyeongbuk Institute of Science and Technology. (C) Schematic diagram for the in vivo experiment. The optogenetic stimulator sheds blue light on the motor cortex, activating Chr2. Inserted multichannel electrodes simultaneously record changes in neural activity in response to optogenetic stimulation with various intensities. (D) Example traces of neural activity with blue light illumination (top) and examples of spike waveforms of isolated units evoked by the  $\mu$ -ILED operation (bottom) (ON, red box; OFF, blue box). (E) Frequency of the firing rate upon optogenetic stimulation at various intensities (0, 2, 6, and 20 mW).

printing, which is affected by uncontrollable fluid flow and chemical diffusion, the dry transfer printing suggested here is a fluid-free process that actively exploits the intrinsic material properties and functional layer. First, the difference between the CTEs of adjacent dissimilar materials creates thermal stress at the heterogeneous interface, which induces interfacial cracks at the edge. Second, the formation of the chemically treated functional layer prevents the atomic diffusion that increases adhesion to the substrate. Through unsophisticated heat treatment, the dry transfer printing provides a rapid release time and deterministic assembly of scalable elements/patterns, which circumvents the main limitations of wet transfer printing. In this method, the metal layer remains attached to the device upon completion of transfer printing. If necessary, this metal

layer can be immediately removed by exposing to an etchant while the device is attached to the adhesion tape. The abovementioned advantages of the proposed method (i.e., the process is instant, deterministic, and scalable) will be maintained even if wet etching is performed before transferring the device to receiver substrate. The FEA of the process feasibility and the working principles of the proposed dry transfer printing reveal the following: (i) The stress is concentrated at the edge of the interface during the heating process; (ii) the CTE mismatch at the heterogeneous interface causes micro-cracks, inducing delamination. These strategies are proven with multi-scale, sequential wet-dry, circuit-level, and biological topography-based transfer printing. The proposed dry transfer printing provides new opportunities for extensive applications of modern electronics in a wide range of areas that have not been addressed with traditional wet transfer printing methods over the past few decades.

## MATERIALS AND METHODS

### Fabrication process of $\mu$ -ILED

The  $\mu$ -ILEDs (300  $\mu\text{m}$  by 300  $\mu\text{m}$  by 2.7  $\mu\text{m}$ ) used in this paper were fabricated with GaAs-based wafers that have epitaxial structures, including Zn-doped layers (50-nm GaAs p-contact/800-nm  $\text{Al}_{0.45}\text{GaAs}$  p-spreader/200-nm  $\text{Al}_{0.33}\text{GaAs}$  p-cladding), quantum well structures [10-nm  $\text{Al}_{0.33}\text{GaAs}$  barrier/4 $\times$  (10-nm GaAs quantum well)/10-nm  $\text{Al}_{0.33}\text{GaAs}$  barrier], Si-doped layers (200 nm  $\text{Al}_{0.33}\text{GaAs}$  n-cladding/800-nm  $\text{Al}_{0.45}\text{GaAs}$  n-spreader/500-nm GaAs n-contact), and sacrificial layers (500-nm  $\text{Al}_{0.95}\text{GaAs}$ ). The fabrication process of the  $\mu$ -ILED began with deposition of  $\text{SiO}_2$  (600 nm in thickness) on a GaAs wafer. The  $\text{SiO}_2$  layer was patterned by photolithography and buffered oxide etching (BOE). To expose the n-contact layer, inductively coupled plasma-reactive ion etching [ICP-RIE;  $\text{Cl}_2$  20 standard cubic centimeters per minute (sccm), 1000 W/100 W] through a photolithographically defined hard mask of  $\text{SiO}_2$  formed a trench down to the n-contact layer. After photolithographically defined PR patterning for protection of the n-contact layer connected to the LED, the residue of the n-contact layer between the devices was removed by a wet etching process ( $\text{H}_3\text{PO}_4\text{:DI:H}_2\text{O}_2 = 1\text{:}12\text{:}13$  for 50 s). PR photopatterning and wet etching of  $\text{SiO}_2$  to expose certain regions of p-contact allowed the formation of non-ohmic metal contacts and interconnections of lines. N-metal contact ( $\text{Pd/Ge/Au} = 5/35/70$  nm) and p-metal contact ( $\text{Pt/Ti/Pt/Au} = 10/40/40/50$  nm) were deposited by electron beam evaporation and patterned by photolithography and liftoff. Last, the photolithographically patterned anchoring PR structures described in fig. S11 held the epitaxial layer to the underlying GaAs wafer during removal of the  $\text{Al}_{0.95}\text{GaAs}$  with diluted hydrofluoric acid (HF) etching solution ( $\text{DI:HF} = 20\text{:}1$  for 2 hours).

### Fabrication process of $\mu$ -Si PD

The  $\mu$ -Si PD (100  $\mu\text{m}$  by 260  $\mu\text{m}$  by 1.25  $\mu\text{m}$ ) used in this paper was fabricated with a silicon on insulator (SOI) wafer that has a phosphorus/boron-doped region with a doping concentration of  $5 \times 10^{19} \text{ cm}^{-3}$  for  $n^+$  and  $p^+$  doping through ion implantation. To isolate the  $\mu$ -Si PD from the substrate, the  $\mu$ -Si PD was patterned by photolithography with a PR (AZ 5214, Microchem) and dry etching using ICP-RIE. In addition, to remove the buried oxide layer, a wet etching process was applied with 49% HF. An anchoring PR was coated, and the sacrificial layer was eliminated by the wet etching process. The detailed steps for the fabrication follow previously reported procedures.

### SAM treatment

The Si substrate was treated with trichloro(1H,1H,2H,2H-perfluorooctyl)silane (Sigma-Aldrich) vapor at room temperature for 2 hours to form an antiatomic diffusion layer.

### Fabrication of the Marilyn Monroe pattern

Sputter deposition (50 W) was used to form a thin Au layer (200 nm) on a temporary Si wafer substrate (150 mm in diameter; 0.625 mm in thickness; <100>). Photolithographic patterning and wet chemical etching were used to define the designed *Marilyn Monroe* geometry. A transparent adhesive allowed thermal exfoliation of the completed pattern from the Si substrate after heating and sequential cooling of the entire pattern.

### Fabrication process for the wireless heater

Surface treatment with trichloro(1H,1H,2H,2H-perfluorooctyl)silane (Sigma-Aldrich) of the Si wafer yielded an antiatomic diffusion layer. Sputter deposition (50 W) was used to form a thin Cu film (100 nm). Spin casting and thermal curing were used to form a layer of PI (3  $\mu$ m in thickness, Sigma-Aldrich). Sputter deposition (200 W/50 W) followed by patterning of metal bilayers of Cr (24 nm)/Au (100 nm) was used to form the serpentine structures for the wireless micro-heater. Selective deposition of the Cu layer (3  $\mu$ m) through the corresponding shadow metal mask was used for the dipole antenna. Another layer of PI (3  $\mu$ m) was spin cast to encapsulate the devices. Reactive ion etching (20 sccm O<sub>2</sub>, 30 mtorr, and 150 W) followed by wet etching was used to remove the PI/Cu. Heating and cooling of the dry transfer printing allowed the devices to be retrieved with a transparent adhesive film.

### Fabrication process of the pulse oximeter

Metal deposition (50 W) yielded a thin Au layer (100 nm) on the Si substrate. A spin cast and partially cured layer of PI (2  $\mu$ m) served as an adhesive. Two  $\mu$ -ILEDs and  $\mu$ -Si PD fabricated according to the procedures described previously were transfer-printed onto the partially cured PI with an elastomeric stamp. The PI was fully cured by heating. Another layer of PI (1.5  $\mu$ m) was spin cast, and photolithographic patterning followed by reactive ion etching (20 sccm O<sub>2</sub>, 30 mtorr, and 150 W) was used to define holes. Sputter deposition (200 W/50 W) and patterning of metal bilayers of Cr (24 nm)/Au (300 nm) was used to form the patterns of the metal interconnects. A film of PI (1.5  $\mu$ m) was spin cast to form a dielectric layer. Reactive ion etching (20 sccm O<sub>2</sub>, 30 mtorr, and 150 W) was used to eliminate the photolithographically unprotected PI regions. Wet etching was used to remove the Au. An induced thermal stress through a dry transfer printing technique was used to retrieve the device layer onto the water-soluble tape (ASWT-2, AQUASOL). Metal layers of Ti (3 nm)/SiO<sub>2</sub> (20 nm) formed by sputter deposition (100 W/100 W) on the surface of water-soluble tape formed siloxane bonds with the ultraviolet (UV)-treated silicone elastomer substrate (Ecoflex 0050, Smooth-on). Dissolving the tape with water and connecting the conductive wires with solder paste (NC-SMQ80, Indium Corporation) completed the fabrication.

### Fabrication process of the ECG sensor

Fabrication began with sputter deposition (50 W) of the Au layer followed by spin casting of the PI layer (1.5  $\mu$ m) on the Si substrate. Photolithographically patterned metal layers of Cr (24 nm)/Au (300 nm) formed by sputter deposition (200 W/50 W) were used for the

electrodes for the ECG sensor. A spin cast and thermally cured second layer of PI served as a passivation layer. Photolithography and reactive ion etching (20 sccm O<sub>2</sub>, 30 mtorr, and 150 W) were used to define the desired open mesh structures. Wet chemical etching of the photolithographically patterned Au and application of thermal stress facilitated the release of the resulting devices with water-soluble tape (ASWT-2, AQUASOL). Sputter deposition (100 W/100 W) of Ti (3 nm)/SiO<sub>2</sub> (20 nm) bilayers on the tape formed siloxane bonds to the silicone substrate (Ecoflex 0030, Smooth-on) before UV radiation treatment.

### Fabrication process of the wireless gas inhale monitor

Sputter deposition (50 W) yielded a copper layer (100 nm) on a silane-functionalized Si substrate. A film of PI (1.5  $\mu$ m) spin cast and baked on Cu established an encapsulation layer. Photolithographic patterning of metal layers of Cr (24 nm)/Au (300 nm) formed by sputter deposition (200 W/50 W) was used to define the conductive traces. The second PI layer (1.5  $\mu$ m) served to isolate the metal traces. Reactive ion etching (20 sccm O<sub>2</sub>, 30 mtorr, and 150 W) was used to create the contact pads as bonding points of electronic components. Wet etching was used to eliminate the exposed Cu layer. Thermal stress induced by heating and cooling enabled the retrieval of the entire structures with water-soluble tape (ASWT-2, AQUASOL) and integration with a PDMS substrate (Dow Corning). A conductive alloy (NC-SMQ80, Indium Corporation) connected the surface-mounted circuit chips to the contact pads of metal traces.

### Fabrication process of the scalp-mounted optogenetic stimulator

Fabrication began with the formation of a thin Au film (100 nm) by sputter deposition (50 W) on a glass substrate. Spin casting and thermal curing yielded a layer of PI (1.5  $\mu$ m). Photolithography with standard PR and reactive ion etching (20 sccm O<sub>2</sub>, 150 W, and 30 mtorr) was used to determine the patterns of the serpentine metal interconnects. Wet chemical etching with Au etchant was used to define the Au configurations. Sticky tape separated the completed patterns from the temporary support after the application of the thermal stress to the entire substrate. Water-soluble tape (ASWT-2, AQUASOL) subsequently enabled the resulting patterns to be retrieved from the sticky tape and delivered them onto a glass substrate coated with bilayers of polymethyl methacrylate (PMMA; PMMA A6 495, Microchem) and PDMS layer (Dow Corning). Dropping water onto the water-soluble tape exposed the contact pads of the LEDs (220  $\mu$ m by 270  $\mu$ m by 50  $\mu$ m; CREE Inc.). Conductive silver epoxy (CW2400, Circuit works) was used to electrically bond the LEDs to the contact pads. An anisotropic conductive film (Elform) was connected to the device to provide an external power supply to the LEDs. The physical separation of the device from the glass substrate completed the process.

### Finite element analysis

3D and 2D FEA were used to predict the thermal stress distribution of the substrate and the device layer during dry transfer printing. Mapped meshes and free triangular 2D meshes were used for the FEA. The meshes around the edge of the interface were formed with extremely high density for calculation accuracy. The device consisted of three layers of Au (200 nm), PI (1  $\mu$ m), and the Cu device layer (200 nm) with a width of 2 cm, and the substrate (100 mm in diameter; 525  $\mu$ m in thickness) consisted of Si. An Al plate (250 mm in width;



3 cm in thickness) was placed under the substrate and acted as a heater and cooler. The initial temperature of the device and substrate was 20°C. The temperature of the Al plate was initially set to 150°C and was changed to 20°C at 3 s. All surfaces in contact with the air were covered with an insulating film, as the heat flux due to convection was negligible compared to the heat flux due to conduction. The residual stress of the interface between the substrate and the device layer was set to zero at the initial temperature of the device and the substrate. The thermal contact condition was used at the interface between the substrate and the Al plate. In Fig. 2A, the contact pair condition was used at the interface between the device layer and substrate for detachment of the meshes. In Fig. 2 (B to D), the contact pair condition was not used, as evaluated by the maximum stress under the no crack initiation condition. Thermal stress analysis was used to determine the spatiotemporal temperature and the corresponding thermal stress. The parameters used in the FEA are listed in table S1.

### Wireless heater system

A network analyzer (E5071C, Keysight Technologies) obtained the scattering parameters ( $S_{11}$ ) and resonance frequency of the RF antennas designed with different antenna lengths. The RF signals were generated by a signal generator (N5182A, Keysight Technologies) and modulated with a power amplifier (FMAM4011, Fairview Microwave) and DC power supply (2401, Keithley). A Yagi antenna with 25 dBi was used to expose the RF power to the fabricated wireless microheater. A thermal imager (A655sc, FLIR) was used to precisely track the changes in the temperature of the heater according to the RF irradiation. A spectrum analyzer (E4405B, Keysight Technologies) measured the absorbed power of the fabricated RF antenna.

### Wireless gas inhalation monitor

Wireless gas inhalation monitor, including an analog accelerometer (ADXL337, Analog Devices) and a microelectromechanical system (MEMS) gas sensor (MICS-6814, SGX Sensortech Limited), measured the signals for the static acceleration of gravity and three types of gases ( $\text{NH}_3$ , CO, and  $\text{NO}_2$ ). The bandwidth of the signal was adjusted below 50 Hz by adding a bypass capacitor (0.1  $\mu\text{F}$ ). An analog multiplexer (TMUX1208, Texas Instruments) was used to select the individual output of carbon monoxide (CO) among the collected signals from the gas sensor. A Bluetooth system (QN9080-001-M17, NXP) acquired raw data from each sensor and wirelessly transmitted the data to a personal PC for signal processing and quantitative analysis.

### Gas inhalation measurements and signal processing

The wireless sensor was attached to a chest of the subject, with a cigarette placed near the sensor. The accelerometer detected the movement of the chest during inhalation and exhalation, and simultaneously, the air quality sensor measured the change in the CO concentration in the surrounding atmosphere. The wireless receiver collected the raw data from each sensor with a sampling frequency of 8 Hz. Substituting the acceleration data obtained as a voltage value into the conversion formula yielded the gravitational acceleration. The converted data were filtered with an eight-point Gaussian window and normalized by setting the maximum value as 1. The respiratory rate per minute was derived from the time interval between the peaks of the acceleration waveform. The acquired voltage values

for the CO concentration were converted into concentration values (parts per million) based on the conversion formula and Gaussian filtering. The total CO inhalation volume was calculated from the respiratory rate and CO concentration.

### ECG, PPG, and PAT analysis

For in vivo measurements, the electrodes of the epidermal EP sensor were attached to the right flank and left and right abdomen of the subject with van der Waals forces. The electrical potential between the electrodes was measured and digitized with a 32-bit analog-to-digital converter (ADC). The ECG signals were collected at a sampling frequency of 50 Hz and high-pass-filtered (0.5 Hz, eighth-order Chebyshev filter) to remove baseline wander using analysis software (MATLAB R2017a, MathWorks Inc.). The PPG sensor was placed on the middle fingertip of the human subject and was compared to a commercial pulse oximeter (MD300C22, ChoiceM Med Inc.). During the test, the subject was relaxed, and data were acquired simultaneously for 30 s. The real-time data collection began with the alternating blinking of the general purpose input/output (GPIO)-controlled two LEDs (switching time, 80 ms; red, 670 nm; IR, 950 nm) and the reflected light sensing of the PD (sampling frequency, 50 Hz). The data collected from the PD went through a series of analog signal processes including analog filters, inversion amplifiers, and a 32-bit ADC in a microcontroller system (QN9080-001-M17, NXP). The PAT was calculated from the time intervals between the simultaneously obtained ECG and PPG signal waveforms.

### Pulse oximeter data analysis

The raw signal of the dry-transferred pulse oximeter from the PD was transmitted from the designed PCB to a personal laptop. The high and low voltages from the raw signal were separated using laboratory-built software (MATLAB R2013b, MathWorks Inc.), where each voltage indicated data for the two optical wavelengths. The separated data were smoothed through convolution with a Gaussian window. Then, the procedure for finding peaks and valleys was executed to extract the pulsatile component (AC) and the non-pulsatile component (DC). These peaks and valleys can be used to measure the heart rate beats per minute (BPM) and the AC/DC ratio of the two signals ( $R$  value), which are related to oxygen saturation ( $\text{SpO}_2$ ). The arterial oxygen saturation was computed from the modified Beer-Lambert equation and photon-diffusion analysis.

### 3D scanning method

A 3D scanner (AICON, SmartScan) was used to scan the topography of the mouse skull model, which was marked with stimulation sites using the triangulation method. The raw scanning data at and adjacent to the stimulation sites were merged using reverse engineering software (Design X, 3D Systems). The distance from the bregma to each target site was expressed as an approximate value by the analysis software (Solidworks, Dassault Systemes).

### In vivo electrophysiological recordings

For the electrophysiological studies, mice were housed under a 12-hour light-dark cycle with freely available food and water. The C57BL/6 mice were injected in the rostral forelimb area (RFA) (AP, +2.0 mm from bregma; ML,  $\pm 0.5$  mm from midline; ML, mediolateral; AP, anteroposterior, relative to bregma) with AAV1-CAG-ChR2-Venus (AAV1.CAG.ChR2-Venus.WPRE.SV40, University of Pennsylvania Vector Core, Philadelphia, PA) (total volume

of 100 nl) under ketamine (100 mg/kg) anesthesia. Three weeks after the AAV injection, the mice were anesthetized with ketamine (100 mg/kg) and placed in a stereotaxic device (World Precision Instruments, Sarasota, FL, USA) for electrophysiological recordings. The body temperature was maintained at 36.5°C by a heating pad. The scalp was incised, and holes were drilled in the skull overlying the site of recording, M2 (AP, +1.6 to 2.0 mm from bregma; L,  $\pm 0.4$  to 0.6 mm from midline at an anteroposterior angle of 30°; and V, 0.7 to 1.0 mm below dura) according to the coordinates from the atlas of Franklin and Paxinos (1997). We performed extracellular recordings using a silicon probe (A1x16-3 mm-100-177-A16, NeuroNexus, Ann Arbor, MI, USA) with 16 channels. The recording electrodes were attached to a micromanipulator and moved gradually to a depth of ~1000  $\mu$ m under the surface. We recorded the band-pass-filtered (0.1 to 7.5 kHz) signals at 30 kHz using an Intan system (RHD 2000 USB interface board, Intan Technologies). Extracellular waveforms were classified as single neurons using an offline sorter (Plexon) with principal component analysis. The neuronal activity was analyzed with NeuroExplorer (NEX Technology, Colorado Springs, CO, USA). All procedures of animal experiments were approved by the Institutional Animal Care and Use Committee. (IACUC-2019-0048).

## SUPPLEMENTARY MATERIALS

Supplementary material for this article is available at <http://advances.sciencemag.org/cgi/content/full/7/28/eabh0040/DC1>

## REFERENCES AND NOTES

- J. A. Rogers, T. Someya, Y. Huang, Materials and mechanics for stretchable electronics. *Science* **327**, 1603–1607 (2010).
- Q. Cao, H. S. Kim, N. Pimparkar, J. P. Kulkarni, C. Wang, M. Shim, K. Roy, M. A. Alam, J. A. Rogers, Medium-scale carbon nanotube thin-film integrated circuits on flexible plastic substrates. *Nature* **454**, 495–500 (2008).
- X. Duan, C. Niu, V. Sahi, J. Chen, J. W. Parce, S. Empedocles, J. L. Goldman, High-performance thin-film transistors using semiconductor nanowires and nanoribbons. *Nature* **425**, 274–278 (2003).
- S. H. Hur, O. O. Park, J. A. Rogers, Extreme bendability of single-walled carbon nanotube networks transferred from high-temperature growth substrates to plastic and their use in thin-film transistors. *Appl. Phys. Lett.* **86**, 243502 (2005).
- M. Kaltenbrunner, T. Sekitani, J. Reeder, T. Yokota, K. Kuribara, T. Tokuhara, M. Drack, R. Schwödiauer, I. Graz, S. Bauer-Gogonea, S. Bauer, T. Someya, An ultra-lightweight design for imperceptible plastic electronics. *Nature* **499**, 458–463 (2013).
- D. H. Kim, J. Song, W. M. Choi, H. S. Kim, R. H. Kim, Z. Liu, Y. Y. Huang, K. C. Hwang, Y. W. Zhang, J. A. Rogers, Materials and noncoplanar mesh designs for integrated circuits with linear elastic responses to extreme mechanical deformations. *Proc. Natl. Acad. Sci. U.S.A.* **105**, 18675–18680 (2008).
- E. Menard, K. J. Lee, D.-Y. Khang, R. G. Nuzzo, J. A. Rogers, A printable form of silicon for high performance thin film transistors on plastic substrates. *Appl. Phys. Lett.* **84**, 5398–5400 (2004).
- E. Menard, R. G. Nuzzo, J. A. Rogers, Bendable single crystal silicon thin film transistors formed by printing on plastic substrates. *Appl. Phys. Lett.* **86**, 093507 (2005).
- C. A. Bower, M. A. Meitl, B. Raymond, E. Radauscher, R. Cok, S. Bonafede, D. Gomez, T. Moore, C. Prevatt, B. Fisher, R. Rotzoll, G. A. Melnik, A. Fecioru, A. J. Trindade, Emissive displays with transfer-printed assemblies of 8  $\mu$ m  $\times$  15  $\mu$ m inorganic light-emitting diodes. *Photonics Res.* **5**, A23–A29 (2017).
- M. Choi, B. Jang, W. Lee, S. Lee, T. W. Kim, H. J. Lee, J. H. Kim, J. H. Ahn, Stretchable active matrix inorganic light-emitting diode display enabled by overlay-aligned roll-transfer printing. *Adv. Funct. Mater.* **27**, 1606005 (2017).
- X. Hu, P. Krull, B. de Graff, K. Dowling, J. A. Rogers, W. J. Arora, Stretchable inorganic-semiconductor electronic systems. *Adv. Mater.* **23**, 2933–2936 (2011).
- R. H. Kim, D. H. Kim, J. Xiao, B. H. Kim, S. I. Park, B. Panilaitis, R. Ghaffari, J. Yao, M. Li, Z. Liu, V. Malyarchuk, D. G. Kim, A. P. Ie, R. G. Nuzzo, D. L. Kaplan, F. G. Omenetto, Y. Huang, Z. Kang, J. A. Rogers, Waterproof AllnGaP optoelectronics on stretchable substrates with applications in biomedicine and robotics. *Nat. Mater.* **9**, 929–937 (2010).
- T.-i. Kim, Y. H. Jung, J. Song, D. Kim, Y. Li, H.-s. Kim, I.-S. Song, J. J. Wierer, H. A. Pao, Y. Huang, J. A. Rogers, High-efficiency, microscale GaN light-emitting diodes and their thermal properties on unusual substrates. *Small* **8**, 1643–1649 (2012).
- H. C. Ko, M. P. Stoykovich, J. Song, V. Malyarchuk, W. M. Choi, C. J. Yu, J. B. Geddes III, J. Xiao, S. Wang, Y. Huang, J. A. Rogers, A hemispherical electronic eye camera based on compressible silicon optoelectronics. *Nature* **454**, 748–753 (2008).
- J. Kim, A. Banks, Z. Xie, S. Y. Heo, P. Gutruf, J. W. Lee, S. Xu, K. I. Jang, F. Liu, G. Brown, J. Choi, J. H. Kim, X. Feng, Y. Huang, U. Paik, J. A. Rogers, Miniaturized flexible electronic systems with wireless power and near-field communication capabilities. *Adv. Funct. Mater.* **25**, 4761–4767 (2015).
- S. Xu, Y. Zhang, J. Cho, J. Lee, X. Huang, L. Jia, J. A. Fan, Y. Su, J. Su, H. Zhang, H. Cheng, B. Lu, C. Yu, C. Chuang, T.-I. Kim, T. Song, K. Shigeta, S. Kang, C. Dagdeviren, I. Petrov, P. V. Braun, Y. Huang, U. Paik, J. A. Rogers, Stretchable batteries with self-similar serpentine interconnects and integrated wireless recharging systems. *Nat. Commun.* **4**, 1543 (2013).
- W. Gao, S. Emaminejad, H. Y. Y. Nyein, S. Challa, K. Chen, A. Peck, H. M. Fahad, H. Ota, H. Shiraki, D. Kiriya, D. H. Lien, G. A. Brooks, R. W. Davis, A. Javey, Fully integrated wearable sensor arrays for multiplexed in situ perspiration analysis. *Nature* **529**, 509–514 (2016).
- K. I. Jang, S. Y. Han, S. Xu, K. E. Mathewson, Y. Zhang, J.-W. Jeong, G.-T. Kim, R. C. Webb, J. W. Lee, T. J. Dawidczyk, R. H. Kim, Y. M. Song, W.-H. Yeo, S. Kim, H. Cheng, S. I. Rhee, J. Chung, B. Kim, H. U. Chung, D. Lee, Y. Yang, M. Cho, J. G. Gaspar, R. Carbonari, M. Fabiani, G. Gratton, Y. Huang, J. A. Rogers, Rugged and breathable forms of stretchable electronics with adherent composite substrates for transcutaneous monitoring. *Nat. Commun.* **5**, 4779 (2014).
- J. Viventi, D. H. Kim, L. Vigeland, E. S. Frechette, J. A. Blanco, Y. S. Kim, A. E. Avrin, V. R. Tiruvadi, S. W. Hwang, A. C. Vanleer, D. F. Wulsk, K. Davis, C. E. Gelber, L. Palmer, J. van der Spiegel, J. Wu, J. Xiao, Y. Huang, D. Contreras, J. A. Rogers, B. Litt, Flexible, foldable, actively multiplexed, high-density electrode array for mapping brain activity in vivo. *Nat. Neurosci.* **14**, 1599–1605 (2011).
- D. H. Kim, N. Lu, R. Ma, Y. S. Kim, R. H. Kim, S. Wang, J. Wu, S. M. Won, H. Tao, A. Islam, K. J. Yu, T. I. Kim, R. Chowdhury, M. Ying, L. Xu, M. Li, H. J. Chung, H. Keum, M. McCormick, P. Liu, Y. W. Zhang, F. G. Omenetto, Y. Huang, T. Coleman, J. A. Rogers, Epidermal electronics. *Science* **333**, 838–843 (2011).
- A. Koh, D. Kang, Y. Xue, S. Lee, R. M. Pielak, J. Kim, T. Hwang, S. Min, A. Banks, P. Bastien, M. C. Manco, L. Wang, K. R. Ammann, K.-I. Jang, P. Won, S. Han, R. Ghaffari, U. Paik, M. J. Slepian, G. Balooch, Y. Huang, J. A. Rogers, A soft, wearable microfluidic device for the capture, storage, and colorimetric sensing of sweat. *Sci. Transl. Med.* **8**, 366ra165 (2016).
- D. Son, J. Lee, S. Qiao, R. Ghaffari, J. Kim, J. E. Lee, C. Song, S. J. Kim, D. J. Lee, S. W. Jun, S. Yang, M. Park, J. Shin, K. Do, M. Lee, K. Kang, C. S. Hwang, N. Lu, T. Hyeon, D. H. Kim, Multifunctional wearable devices for diagnosis and therapy of movement disorders. *Nat. Nanotechnol.* **9**, 397–404 (2014).
- J. Viventi, D.-H. Kim, J. D. Moss, Y.-S. Kim, J. A. Blanco, N. Annetta, A. Hicks, J. Xiao, Y. Huang, D. J. Callans, J. A. Rogers, B. Litt, A conformal, bio-interfaced class of silicon electronics for mapping cardiac electrophysiology. *Sci. Transl. Med.* **2**, 24ra22 (2010).
- R. C. Webb, A. P. Bonifas, A. Behnaz, Y. Zhang, K. J. Yu, H. Cheng, M. Shi, Z. Bian, Z. Liu, Y. S. Kim, W. H. Yeo, J. S. Park, J. Song, Y. Li, Y. Huang, A. M. Gorbach, J. A. Rogers, Ultrathin conformal devices for precise and continuous thermal characterization of human skin. *Nat. Mater.* **12**, 938–944 (2013).
- W. H. Yeo, Y. S. Kim, J. Lee, A. Ameen, L. Shi, M. Li, S. Wang, R. Ma, S. H. Jin, Z. Kang, Y. Huang, J. A. Rogers, Multifunctional epidermal electronics printed directly onto the skin. *Adv. Mater.* **25**, 2773–2778 (2013).
- A. Carlson, A. M. Bowen, Y. Huang, R. G. Nuzzo, J. A. Rogers, Transfer printing techniques for materials assembly and micro/nanodevice fabrication. *Adv. Mater.* **24**, 5284–5318 (2012).
- C. Linghu, S. Zhang, C. Wang, J. Song, Transfer printing techniques for flexible and stretchable inorganic electronics. *npi Flex. Electron.* **2**, 26 (2018).
- M. A. Meitl, Z. T. Zhu, V. Kumar, K. J. Lee, X. Feng, Y. Y. Huang, I. Adesida, R. G. Nuzzo, J. A. Rogers, Transfer printing by kinetic control of adhesion to an elastomeric stamp. *Nat. Mater.* **5**, 33–38 (2006).
- Y. Sun, J. A. Rogers, Fabricating semiconductor nano/microwires and transfer printing ordered arrays of them onto plastic substrates. *Nano Lett.* **4**, 1953–1959 (2004).
- H. Luo, C. Wang, C. Linghu, K. Yu, C. Wang, J. Song, Laser-driven programmable non-contact transfer printing of objects onto arbitrary receivers via an active elastomeric micro-structured stamp. *Natl. Sci. Rev.* **7**, 296–304 (2019).
- C. Wang, C. Linghu, S. Nie, C. Li, Q. Lei, X. Tao, Y. Zeng, Y. Du, S. Zhang, K. Yu, H. Jin, W. Chen, J. Song, Programmable and scalable transfer printing with high reliability and efficiency for flexible inorganic electronics. *Sci. Adv.* **6**, eabb2393 (2020).

32. Y.-S. Kim, J. Lu, B. Shih, A. Gharibans, Z. Zou, K. Matsuno, R. Aguilera, Y. Han, A. Meek, J. Xiao, M. T. Tolley, T. P. Coleman, Scalable manufacturing of solderable and stretchable physiologic sensing systems. *Adv. Mater.* **29**, 1701312 (2017).
33. S. J. Kim, H. E. Lee, H. Choi, Y. Kim, J. H. We, J. S. Shin, K. J. Lee, B. J. Cho, High-performance flexible thermoelectric power generator using laser multiscanning lift-off process. *ACS Nano* **10**, 10851–10857 (2016).
34. J. Chang, T. Young, Y. Yang, H. Ueng, T. Chang, Silicide formation of Au thin films on (100) Si during annealing. *Mater. Chem. Phys.* **83**, 199–203 (2004).
35. N. Mikami, N. Hata, T. Kikkawa, H. Machida, Robust self-assembled monolayer as diffusion barrier for copper metallization. *Appl. Phys. Lett.* **83**, 5181–5183 (2003).
36. D. J. Monk, D. S. Soane, R. T. Howe, Hydrofluoric acid etching of silicon dioxide sacrificial layers: II. Modeling. *J. Electrochem. Soc.* **141**, 270–274 (1994).
37. I. B. Mirman, Effects of peeling stresses in bimaterial assembly. *J. Electron. Packag.* **113**, 431–433 (1991).
38. A. Griffith, J. J. Gilman, The phenomena of rupture and flow in solids. *Trans. ASM* **61**, 855–906 (1968).
39. S. I. Park, Y. Xiong, R. H. Kim, P. Elvikis, M. Meitl, D. H. Kim, J. Wu, J. Yoon, C. J. Yu, Z. Liu, Y. Huang, K. C. Hwang, P. Ferreira, X. Li, K. Choquette, J. A. Rogers, Printed assemblies of inorganic light-emitting diodes for deformable and semitransparent displays. *Science* **325**, 977–981 (2009).
40. Y. M. Song, Y. Xie, V. Malyarchuk, J. Xiao, I. Jung, K. J. Choi, Z. Liu, H. Park, C. Lu, R. H. Kim, R. Li, K. B. Crozier, Y. Huang, J. A. Rogers, Digital cameras with designs inspired by the arthropod eye. *Nature* **497**, 95–99 (2013).
41. J. M. Schmitt, Simple photon diffusion analysis of the effects of multiple scattering on pulse oximetry. *I.E.E.E. Trans. Biomed. Eng.* **38**, 1194–1203 (1991).
42. Z. V. Guo, N. Li, D. Huber, E. Ophir, D. Gutnisky, J. T. Ting, G. Feng, K. Svoboda, Flow of cortical activity underlying a tactile decision in mice. *Neuron* **81**, 179–194 (2014).

#### Acknowledgments

**Funding:** This research was supported by multiple grant programs, NRF-2020R1C1C1013030, NRF-2017M3A7B4049476, NRF-2018M3C7A1047342, NRF-2019M3C1B8090845, NRF-2017M3A9G8084463, KGC1022012, 20-BR-04-01, 20-BR-01-01, MOTIE 20006400, and R&D Program for Forest Science Technology (project no. 2021396B10-2123-0107), from the Korean Government. **Author contributions:** K.-I.J., H.K., J.-C.R., S.H., and J.H. designed the project; S.H., J.H., I.S.C., S.J.S., H.L., S.O., and J.J. carried out experiments and analyzed the experimental data; and K.-I.J., H.K., and J.-C.R. supervised the project. All of the coauthors contributed to writing the manuscript. **Competing interests:** The authors declare that they have no competing interests. **Data and materials availability:** All data needed to evaluate the conclusions in the paper are present in the paper and/or the Supplementary Materials. Additional data related to this paper may be requested from the authors.

Submitted 10 February 2021

Accepted 27 May 2021

Published 9 July 2021

10.1126/sciadv.abh0040

**Citation:** S. Heo, J. Ha, S. J. Son, I. S. Choi, H. Lee, S. Oh, J. Jekal, M. H. Kang, G. J. Lee, H. H. Jung, J. Yea, T. Lee, Y. Lee, J.-W. Choi, S. Xu, J. H. Choi, J.-W. Jeong, Y. M. Song, J.-C. Rah, H. Keum, K.-I. Jang, Instant, multiscale dry transfer printing by atomic diffusion control at heterogeneous interfaces. *Sci. Adv.* **7**, eabh0040 (2021).



## Instant, multiscale dry transfer printing by atomic diffusion control at heterogeneous interfaces

Seungkyoung Heo, Jeongdae Ha, Sook Jin Son, In Sun Choi, Hyeokjun Lee, Saehyuck Oh, Janghwan Jekal, Min Hyung Kang, Gil Ju Lee, Han Hee Jung, Junwoo Yea, Taeyoon Lee, Youngjeon Lee, Ji-Woong Choi, Sheng Xu, Joon Ho Choi, Jae-Woong Jeong, Young Min Song, Jong-Cheol Rah, Hohyun Keum and Kyung-In Jang

*Sci Adv* 7 (28), eabh0040.  
DOI: 10.1126/sciadv.abh0040

### ARTICLE TOOLS

<http://advances.sciencemag.org/content/7/28/eabh0040>

### SUPPLEMENTARY MATERIALS

<http://advances.sciencemag.org/content/suppl/2021/07/02/7.28.eabh0040.DC1>

### REFERENCES

This article cites 42 articles, 8 of which you can access for free  
<http://advances.sciencemag.org/content/7/28/eabh0040#BIBL>

### PERMISSIONS

<http://www.sciencemag.org/help/reprints-and-permissions>

Use of this article is subject to the [Terms of Service](#)

*Science Advances* (ISSN 2375-2548) is published by the American Association for the Advancement of Science, 1200 New York Avenue NW, Washington, DC 20005. The title *Science Advances* is a registered trademark of AAAS.

Copyright © 2021 The Authors, some rights reserved; exclusive licensee American Association for the Advancement of Science. No claim to original U.S. Government Works. Distributed under a Creative Commons Attribution NonCommercial License 4.0 (CC BY-NC).